American Society of Mechanical Engineers

ASME Accepted Manuscript Repository

Institutional Repository Cover Sheet

Weeratunga   Malalasekera

First   *Last*

ASME Paper Title: Large eddy simulation of scalar mixing in jet in a cross-flow

Authors:
Uyanwaththa, Asela R.
Malalasekera, W.
Hargrave, Graham K.
Dubal, Mark R.

Large Eddy Simulation of Scalar Mixing in Jet in a Cross-flow.

Asela Uyanwaththa
School of Mechanical, Electrical and Manufacturing Engineering
Loughborough University
UK
Email: a.r.uyanwaththa@lboro.ac.uk

Weeratunge. Malalasekara[*]
School of Mechanical, Electrical and Manufacturing Engineering
Loughborough University
UK Email: w.malalasekara@lboro.ac.uk

Graham Hargrave
School of Mechanical, Electrical and Manufacturing Engineering
Loughborough University
UK
Email:G.K.Hargrave@lboro.ac.uk

Mark Dubal
Uniper Technologies Limited
Technology Centre
Ratcliffe-on-Soar
Nottinghamshire
NG11 0EG
UK
Email:Mark.Dubal@uniper.energy

ABSTRACT

Jet in a Cross-Flow (JICF) is a flow arrangement found in many engineering applications, especially in gas turbine air-fuel mixing. Understanding of scalar mixing in JICF is important for low NO_x burner design and operation, and numerical simulation techniques can be used to understand both spatial and temporal variation of air-fuel mixing quality in such applications. In this paper mixing of the jet stream with the cross-flow is simulated by approximating the jet flow as a passive scalar and using the Large Eddy Simulation (LES) technique to simulate the turbulent velocity field. A posteriori test is conducted to assess three dynamic Sub-Grid Scale models in modelling jet and cross-flow interaction with the boundary layer flow field. Simulated mean and Reynolds stress component values for velocity field and concentration fields are compared against experimental data to assess the capability of the LES technique, which showed good agreement between numerical and experimental results. Similarly, time mean and RMS values of passive scalar concentration also showed good agreement with experimental data. In addition, LES results are further used to discuss the scalar mixing field in the downstream mixing region.

Nomenclature
JICF   Jet In Cross-flow

---

[*]Address all correspondence related to ASME style format and figures to this author.

J Momentum Ratio
k Turbulent Kinetic Energy
R Velocity Ratio
Sc_t Turbulent Schmidt Number
Sc Schmidt Number
ν_{sgs} Sub-Grid viscosity
ε Turbulent Kinetic Energy Dissipation Rate
LIF Laser Induced Fluorescence
$PLIF$ Planar Laser Induced Fluorescence
PIV Particle Image Velocimetry
$\overline{C'}$ Passive scalar standard deviation
δ_{ij} Dirac delta function
Δ Grid filter size
CVP Counter-rotating Vortex Pair
V_j Jet Flow Velocity
V_{cf} Cross-Flow Velocity
U, V, W Velocity components in x,y,z directions

1   Introduction

Fuel jet injection into swirling/non-swirling cross-flow is a commonly used air-fuel premixing technique in low NO_x gas turbine burners, and it is known that both temporal and spatial fluctuations of air-fuel mixing quality affect the NO_x emission levels [1]. Fric [2] showed that even small temporal fluctuations could cause a significant increase in NO_x production in premixed burners. Therefore, investigations of air-fuel mixing methods are vital for future low emission gas turbine designs as there is increasing requirement to achieve low emission levels. The flow configuration where a secondary flow (fuel jet) injecting into a stream of air is common in gas turbine air-fuel mixing arrangements and this flow situation can be simply classified as a Jet In Cross-Flow (JICF) arrangement. In a practical gas turbine, air-fuel mixing arrangments multiple fuel injection nozzles are used. JICF induces a highly turbulent velocity field with vortical structures formed from the interaction between jet flow and cross-flow in addition to flow interaction with the boundary layer. These complex vortical structures cause air-fuel mixing non-uniformities and therein lies the need for analysis of scalar mixing in JICF arrangements.

Early research on JICF studies have been mainly encouraged by the short takeoff/vertical landing (STOVL) aircraft developments [3], also JICF can be found in film cooling of gas turbine blades and impingement cooling applications [4, 5]. Different jet penetration levels are required according to the anticipated end purpose. In mixing applications, a uniform mixing field is required, whereas in film cooling applications the jet is expected to remain attached to the wall. Different jet penetration levels are obtained by changing the momentum ratio (J) and velocity ratio (R) according to the application. Therefore the momentum ratio (J) and velocity ratio (R) for mixing applications are greater than film cooling applications but lower than impingement cooling applications. In general JICF problems are classified by velocity ratio, and momentum ratio between the jet stream and cross-flow stream. The Reynolds number (**Re**) is also used to define JICF problems.

$$R = \frac{V_j}{V_{cf}}, \quad J = \frac{\rho_j V_j^2}{\rho_{cf} V_{cf}^2} \tag{1}$$

1.1   Previous experimental studies

Many experimental studies on JICF are reported in the literature with varying experimental conditions related to different applications. JICF experiments related to gas turbine fuel injection are usually with high-velocity ratios ($R = 1 - 10$) and high Reynolds numbers, while low-velocity ratio experiments ($R < 1$) are aimed toward thin film cooling applications, and $R > 10$ flows resemble impingent cooling applications [6]. Therefore selecting a suitable experimental case for posteriori testing of LES requires careful consideration. Here we summarise a few prominent experimental and numerical analysis works related to turbulent JICF studies that can be used for numerical model validations. Keffer and Baines [7] conducted experimental studies on a circular jet in cross-flow problems using hot-wire anemometry and smoke visualisation. They found that the JICF arrangement does not produce entirely self-preserving flow structure like in turbulent jets because JICF produces stronger turbulence flow structures downstream. Experimental work by Ramsey and Goldstein [8] carried out a comprehensive study using hot-wire anemometry measurements and flow visualisation of JICF arrangements with low-velocity ratios that can be used in film cooling applications. By extending the work of Keffer and Bains, Kamotani et al. [9] performed JICF experiments for high momentum ratios varying from $J = 15 - 60$. Mean velocity measurements and temperature distribution measurements for a hot jet injection was reported by them using hot-wire anemometry and thermocouple measurements. Crabb et al. [10] performed velocity field measurements of JICF with velocity ratios $R = 1.15$

and $R = 2.3$ using Laser Doppler Anemometry in the field near the jet exit and hot wire anemometry in the far field; further they measured jet flow concentration using Helium tracers. Their experimental data provided mean velocity field data and Reynolds stress component data.

Andreopoulos and Rodi conducted experiments on low-velocity ratio JICF arrangements (R = 0.5, 1.0, 2.0) using three hot-wire probes, and recorded mean velocity components, turbulent kinetic energy data and three Reynolds shear stress component measurements [11]. Their measurements indicated the presence of three distinct turbulent kinetic energy regions, first over the jet exit where turbulence is generated from strong velocity gradients and curvature, the second region immediately downstream where the velocity gradient normal to the wall produces kinetic energy, and thirdly further downstream where turbulence decays as velocity gradients attenuate. Importantly their work observed that the flow inside the pipe that carries the jet stream is affected by cross-flow velocities and this phenomenon becomes an important consideration when inlet boundary conditions are treated in unsteady JICF simulations. Smith and Mungal [12] performed passive scalar mixing experiments in JICF at different velocity ratios varying from 6-14 using Planar Laser-Induced Fluorescence technique, and later extended their investigations to velocity ratios ranging from $R = 5$ to 25 [13]. Their study showed that for very high-velocity ratios (R = 10 - 25), the flow features are consistent and can be divided into two regions, near flow field and far field based on the scalar concentration decay rate. They further showed that the Counter Rotating Vortex Pair (CVP) generated from the interaction between jet and crossflow develop in the near field, and progress to be fully developed in the far field. Later Su and Mungal [14] performed simultaneous measurements of the scalar field and 2-D velocity field using PLIF and Particle Image Velocimetry (PIV) for ($R = 5.7$) and focused on the flow developing near field.

Cárdenas et al. [15], used a combination of 2D-LIF and PIV method, to simultaneously measure the Reynolds stress fields and scalar concentration fields. This experimental setup was later used by Galeazzo et al. [16] to measure JICF of $R = 4.15$. Later Cárdenas et al. [17] performed improved measurements with accurate inlet boundary conditions of the same velocity ratio $R = 4.15$ to measure the scalar mixing field and the Reynolds stress field. Their experimental work was particularly focused on air-fuel mixing applications and was performed at high Re number flow conditions. This experimental setup has been used with different velocity ratios for numerical model validation purposes and analysis of scalar mixing in a number of studies [18–20]. Therefore for this work, experimental data were carefully extracted from Galeazzo et al. [16, 18], and Cárdanes et al. [17]. Although these two experiments were performed separately, the velocity ratios and inlet turbulence levels were maintained at the same level.

1.2 Previous numerical simulations

One of the earliest computational fluid dynamic analysis of the JICF problem was performed by Patankar et al. [21] in which the standard $k - \varepsilon$ model was used for turbulence closure, and their predictions showed moderate agreement with experimental mean velocity measurements in the cross-flow direction. A more comprehensive computational study of JICF was performed by Alvarez et al. [22] using the $k - \varepsilon$ model and a second-moment closure model, in which they numerically modelled the experimental test cases by Andreapolous and Rodi [11], Ramsey and Goldstein [8]. In their work scalar transport was modelled using the scalar flux transport closure method proposed by Launder and Samaraweera [23]. From their work the second moment closure model showed slightly better agreement with experimental results compared to the $k - \varepsilon$ model especially near the wall, however apart from mean velocity components both models did not predict the turbulent statistics of velocity field or scalar field accurately. More importantly, the turbulent kinetic energy predictions showed poor agreement with experimental results. Similarly, scalar field results also showed disparity probably caused by the poor velocity field agreement. However, the grid size used in this study was nearly 64×10^3 which was not sufficient to draw conclusions on the performance of RANS modelling ability for the JICF problem.

Initial LES work on JICF was performed by Jones and Wille [24] in which they compared three Sub Grid-scale Stress (SGS) Models namely the standard Smagorinsky [25] model with a constant model coefficient, a dynamic Smagorinsky model [26] and a model with one transport equation for sub-grid kinetic energy [27]. They compared the results with the plane jet in cross-flow experimental case by Chan and Hwang [28]. Their work used both adaptive and non-adaptive grids and concluded that mesh adaptation did not result in a significant improvement of results. All three SGS models performed in nearly the same manner in predicting the velocity field despite differences in turbulent eddy viscosity values. However, the model with the transport equation for sub-grid kinetic energy exhibited improved predictions of turbulent quantities in the streamwise direction. The dynamic model showed only localised regions with larger eddy viscosity while other models showed substantial downstream regions with larger eddy viscosity values. Later, an LES study on JICF was conducted by Yuan et al. [29] for two velocity ratios of $R = 2.0$ and $R = 3.3$ in which the experimental case of Sherif and Pletcher [30] was modelled using a locally dynamic SGS model [31] that has shown to be capable of modelling transitional flows and the energy backscatter from unresolved sub-grid scales to resolved scales. Their LES results agreed well with experimental measurements of the velocity field, and the work was more focused on the vortex structure identification. Schlüter and Schönfeld [6] modelled the JICF mixing of a passive scalar using LES methods and validated against a few experimental configurations using two SGS models; Standard Smagorinsky model and a filtered Smagorinsky model. Their results showed that the filtered Smagorinsky model predictions are in better agreement with experimental results than the

3

standard Smagorinsky model. However, these SGS model comparisons were performed with limited data on mean velocity field and turbulent kinetic energy measurements, thus highlighting the need for more comprehensive experimental data for numerical model validation. Majander and Sikkonen [32] investigated the effect of steady and unsteady inlet boundary conditions using the constant coefficient Smagorinsky model and showed very little difference between these two methods, but the unsteady inlet boundary conditions resulted in a stronger flow reversal at the leeward side of the jet. Salewski et al. [33] performed LES without a SGS model by assuming negligible sub-grid energy, and produced comparable numerical predictions with experimental data.

Galeazzo et al. [16] used the simultaneous velocity and scalar field measuring arrangement by Cárdanes et al. [15] and compared LES and RANS simulations for a JICF test case ($R = 4.15$), and showed the superiority of LES results over RANS results especially in the prediction of Reynolds stress terms. Also the $k - \omega$-SST model showed better results in mean velocity field predictions than the $k - \varepsilon$ model. In another attempt to compare the dynamic Smagorinsky model performance and an unsteady $k - \omega$-SST model performance; Galeazzo et al. [34] modelled the same experimental configuration and showed that the dynamic Smagorinsky model results capture the scalar mixing field better than URANS results because LES resolves the scalar transport by vortex structures better than URANS simulations. In this paper data from the same experimental configuration of Galeazzo et al. [16, 18] Cárdanes et al. [17] are used.

1.3 Objectives

The primary objective of this study was to investigate the mixing quality of a jet in a cross-flow arrangement as a prior study to simulating complex gas turbine air-fuel mixing arrangements. In this endeavour the Large Eddy Simulation (LES) technique with dynamic Sub-Grid Scale (SGS) models are used in analysing the velocity field and scalar mixing field. Particular emphasis is placed on assessing LES capabilities for the modelling of mixing field. The open source code OpenFOAM provides LES modelling capabilities, and this work was used to validate OpenFOAM LES models as well. Further, the relationship between large coherent structures and scalar mixing quality are investigated in this study.

2 Governing equations

The fundamental idea behind the LES method is to resolve anisotropic energy containing larger eddies and model isotropic low energy smaller eddies, and in most practical LES studies implicit filtered LES method is used. Filtered continuity and momentum equations for incompressible flow are given by Eqn:(2) and Eqn:(3). The Sub-Grid Stress term τ_{ij} requires closure and it is modelled using Sub-Grid Stress (SGS) models to account for the filtered out eddies.

$$\frac{\partial \overline{u}_i}{\partial x_i} = 0 \tag{2}$$

$$\frac{\partial \overline{u}_i}{\partial t} + \frac{\partial (\overline{u}_i \overline{u}_j)}{\partial x_j} = -\frac{\partial \overline{p}}{\partial x_i} + \frac{\partial}{\partial x_i} \left[\nu \left(\frac{\partial \overline{u}_i}{\partial x_j} + \frac{\partial \overline{u}_j}{\partial x_i} \right) - (\overline{u_i u_j} - \overline{u}_i \overline{u}_j) \right],$$

$$\tau_{ij} = \overline{u_i u_j} - \overline{u}_i \overline{u}_j, \text{resolved strain rate} \quad \overline{S}_{ij} = \frac{1}{2} \left(\frac{\partial \overline{u}_i}{\partial x_j} + \frac{\partial \overline{u}_j}{\partial x_i} \right) \tag{3}$$

2.1 Sub-Grid Stress (SGS) models

In this study, three different dynamic SGS models are compared. Most commonly used SGS models use the analogy between viscous stress and eddy viscosity, hence using the Boussinesq assumption (Eqn:(4)) in which Sub-Grid eddies are assumed to be isotropic,

$$\tau_{ij} = -2 (C_s \Delta)^2 |\overline{S}| \overline{S}_{ij} + \frac{1}{3} \delta_{ij} \tau_{kk}. \tag{4}$$

The well known Smagorinsky model [25], which assumes the local equilibrium of sub-grid scale kinetic energy production and dissipation uses a constant model coefficient C_s Eqn: (5).

$$\mu_{sgs} = (C_s \Delta)^2 |\overline{S}|, \ |\overline{S}| = \sqrt{2 \overline{S}_{ij} \overline{S}_{ij}}. \tag{5}$$

Germano et al. [35] introduced a procedure to dynamically calculate the Smagorinsky model constant, by using the identity between Sub-Grid stresses at two different filter sizes and the resolved stress field.

In the dynamic Smagorinsky-Lilly model implementation the relationship between explicitly calculable resolved turbulent stress L_{ij}, and the test filtered grid stress T_{ij} and SGS stress is given as Eqn:(6)

$$\underbrace{\widetilde{\overline{u_i u_j}} - \widetilde{\overline{u}_i}\widetilde{\overline{u}}_j}_{L_{ij}} = \underbrace{\widetilde{\overline{u_i u_j}} - \widetilde{\overline{u}}_i\widetilde{\overline{u}}_j}_{T_{ij}} - \widetilde{\tau}_{ij}, \tag{6}$$

in which the~operator denotes the test filtering which is taken as twice the size of grid filter scale. In this work the least square method of finding the local Smagorinsky constant proposed by Lilly [36] was used, and this locally dynamic Smagorinsky model is referred to as the DSM. This approach allows calculation of the model coefficient locally using the resolved velocity field, and it is possible to model turbulent energy backscatter via a negative model coefficient.

Based on the notion that smallest resolved eddies and largest unresolved eddies show similarities, scale similarity models have been derived, but these models lack turbulence dissipation. Therefore, Zang et.al [31] proposed the mixed model that incorporate scale similarity assumption and eddy viscosity assumption to calculate SGS stress as Eqn:(7),

$$\tau_{ij} = (\overline{\overline{u}_i \overline{u}_j} - \overline{\overline{u}_i \overline{u}_j}) - 2C_s^2 \overline{\Delta}^2 \left|\overline{S}\right| \overline{S}_{ij} + \frac{1}{3}\delta_{ij}\tau_{kk}. \tag{7}$$

Vreman et al. [37] proposed an alternative formulation of the mixed model to eliminate mathematical inconsistencies and the model constant was determined dynamically using Lilly's approach, and this Dynamic Mixed Model is referred to as DMM in this paper. In addition to using the scale similarity assumption, this model does not require alignment of the principal axis of turbulent stress tensor and strain tensor. Furthermore, the turbulent energy backscatter can be modelled without introducing negative sub-grid viscosity, therefore increasing the numerical stability. The DMM used in this paper was developed in the OpenFOAM framework by Kornev et.al [38].

Although sub-grid eddies can be assumed to be isotropic and are in equilibrium between sub-grid turbulence generation and dissipation, in the wall boundary layers and at sudden expansion regions these assumptions become invalid; hence SGS models with only the eddy viscosity hypothesis fail to solve the velocity field in such applications accurately. Therefore, instead of assuming the local equilibrium between sub-grid turbulence production and dissipation, a transport equation for the sub-grid kinetic energy (Eqn:(8))can be used with model coefficients C_k, C_ε. The model coefficients are locally calculated using a dynamic procedure proposed by Furby et al. ([39]-(Model B3)). In this work, the Dynamic One-Equation Model is referred to as DOEM,

$$\frac{\partial k_{sgs}}{\partial t} + \frac{\partial(\overline{u}_j k_{sgs})}{\partial x_j} = -\tau_{ij}\frac{\partial \overline{u}_i}{\partial x_j} + \left[(\nu + \nu_{sgs})\frac{\partial k_{sgs}}{\partial x_j}\right] - \varepsilon,$$

$$\tau_{ij} = -2\nu_{sgs}\overline{S}_{ij} + \frac{2}{3}\delta_{ij}k_{sgs}, \tag{8}$$

$$\nu_{sgs} = C_k \Delta \sqrt{k}, \quad \varepsilon = \frac{C_\varepsilon k_{sgs}^{3/2}}{\Delta}.$$

2.2 Passive scalar transport

The jet flow in the experimental study by Galeazzo et al. [16] which is considered in this numerical analysis was seeded with aerosol particles (diethyl-hexyl sebacate DEHS) for the PIV measurements, and for LIF measurements NO_2 was added with 5000 ppm. Therefore the jet flow can be assumed as a flow with a passive scalar, in which the scalar concentration does not affect the velocity field. A filtered passive scalar transport equation for the jet flow can be written as Eqn:(9),

$$\frac{\partial \overline{C}}{\partial t} + \frac{\partial \overline{u}_j \overline{C}}{\partial x_j} = \frac{\partial}{\partial x_i}\left(\frac{\nu}{Sc}\frac{\partial \overline{C}}{\partial x_i}\right) - \frac{\partial}{\partial x_j}\left(\overline{u_i C} - \overline{u}_i \overline{C}\right). \tag{9}$$

The Sub-Grid Scalar flux is modelled using the Gradient Diffusion Hypothesis as,

$$\overline{u_i C} - \overline{u}_i \overline{C} = -\frac{\nu_{sgs}}{Sc_t}\frac{\partial \overline{C}}{\partial x_i}, \tag{10}$$

and the molecular Schmidt number of air Sc was taken as equal to the Prandtl number of air at atmospheric pressure and temperature $300K$ (i.e $Sc = 0.7$). Turbulent Schmidt number Sc_t was set to 0.9.

5

3 Numerical setup

The open source code OpenFOAM was used for these numerical simulations. The incompressible flow solver was used in combination with an additional passive scalar transport equation. The PISO algorithm was used to solve pressure-velocity coupling with correction steps for the non-orthogonality caused by the grid. A second-order implicit scheme was used for temporal discretisation, and a second-order accurate van Leer TVD scheme was used for convection terms. During the calculation, a local Courant number of 0.4 was maintained by controlling the time step ($\Delta t \sim 1 \times 10^{-6}$). A hexahedral computational mesh was used with a very uniform mesh near the jet and cross-flow interaction region. Upstream sides for both cross-flow and jet flow were extended to facilitate the development of the inlet turbulent velocity fields because the experimental details specified fully developed flow profiles [18]. Figure 1 shows an outline of the computational domain. Towards the outlet the cross-flow mesh was expanded to reduce the reverse flow, this method can be justified because the outlet boundary is placed at a 30D distance from the jet centre line. Table 1 shows the boundary measurements at inlets [18]. x, y, z directions are aligned in the cross-flow direction, the spanwise direction of the channel and the jet flow direction respectively. U, V, W are the velocity components in x, y, z directions.

Table 1: Boundary Conditions [16]

	Bulk Velocity	37.72 ms^{-1}
Jet Flow	Turbulent Intensity	7 %
	Re	1.92×10^4
	Bulk Velocity	9.08 ms^{-1}
Cross Flow	Turbulent Intensity	1.5 %
	Re	6.24×10^4
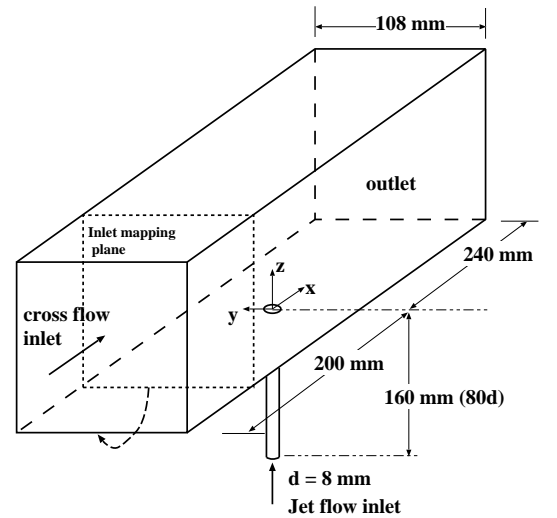
Fig. 1: Computational domain.

3.1 Boundary conditions

In LES eddies smaller than the filter are filtered out, and the larger eddies are required to be specified at the inlet boundaries to accurately represent the inflow conditions. There are different methods of specifying turbulent inflow fluctuations that resembles the spatial and temporal correlations of eddies larger than the grid filter size [40]. Due to the lack of time evolving experimental data at the inlet conditions, a "recycling" method was used to generate the effects of inlet turbulence. In this method, the velocity of the inlet boundary was mapped from an internal plane, where turbulent fluctuations were generated from the boundary layer turbulence. Figure 1 shows this concept in which the cross-flow inlet is mapped from an internal plane, and Figure 3 shows the instantaneous turbulent velocity field at the upstream distance $x = -4D$ that was used to map the cross-flow inlet boundary. At wall boundaries, Spalding's continuous wall function [41] was used in all three simulations. In all three SGS model simulations, the average y^+ value in the pipe flow was nearly 15 and the channel flow y^+ was close to 20. At the outlet boundary, Neumann boundary condition was used with zero gradients.

4 Results

Instantaneous LES velocity and scalar fields were time averaged for $0.15 s$ to compare with experimental results. Time averaging was performed after more than 10 flow passes to remove the effects of initial conditions. U_{cross} was defined as the maximum U velocity component at $x/D = -1.5D$, to obtain dimensionless parameters. To investigate the sensitivity of LES resolution, three computational domains were used; coarse, medium and fine grids consisted of $4.8 \times 10^6, 6.4 \times 10^6$ and 11.0×10^6 cells. Figure 2 shows the results of the mean velocity component in the cross-flow direction at $x = 0.5D$ for the three grids and show that the fine grid solution agrees best with experimental results. Although results from the lesser cell count grids also show good agreement with experimental results at this location, when overall flow field is considered the fine
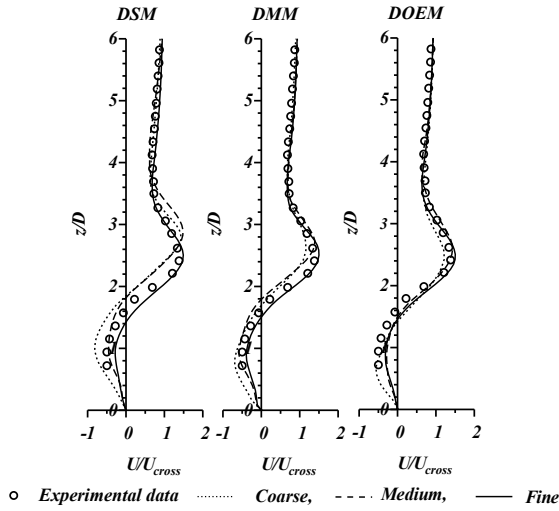
6

Fig. 2: Mesh sensitivity of three SGS models compared at $x = 0.5D$ (Experimental data : [16])
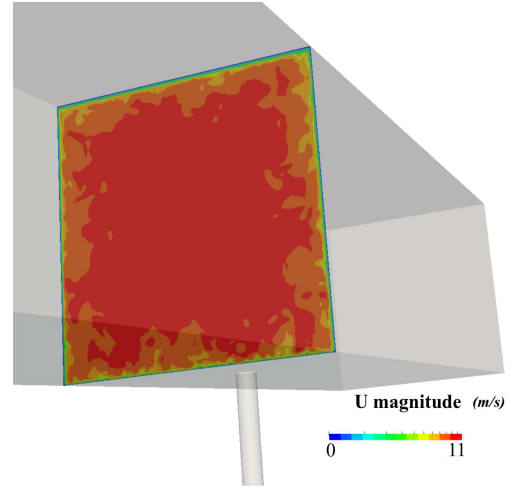

Fig. 3: Upstream instantaneous velocity field.

grid solution showed better agreement with experimental data. In implicit filtered LES solutions the grid resolution is related to the solution resolution, therefore resolved turbulent kinetic energy percentage γ is used to estimate the LES resolution. The idea behind this estimation method is that the grid should be sufficient to produce greater resolved turbulent kinetic energy (k_{res} compared to the modelled sub-grid turbulent kinetic energy (k_{sgs}). Pope [42] suggested $\gamma \geqslant 80\%$ to obtain accurate LES results. γ is calculated using the sub-grid SGS tensor and resolved Reynolds stress tensor as Eqn:(11). All three SGS models achieved more than $\gamma \geqslant 85\%$ in critical areas in the fine mesh solution, and Figure 4a shows the resolved turbulent kinetic energy percentage for the dynamic Smagorinsky model. The other two grid solutions resulted in less than 75% and 70% resolved turbulent kinetic energy percentage; therefore the solutions using 11×10^6 grid are discussed henceforward. Furthermore, Figure 4b shows the difference between the resolved Reynolds stress (T_{ij}) and total Reynolds stress ($T_{ij} + \tau_{ij}$) at $x = 0.5D$, and it can be seen that the effect of sub-grid stress (τ_{ij}) is negligible even at this highly strained location. Therefore in this discussion, the resolved Reynolds stress is assumed to be equal to total Reynolds stress.

$$\gamma = \frac{k_r}{k_{sgs} + k_r} \times 100\%$$

$$k_{sgs} = \frac{1}{2}\langle \tau_{ii} \rangle, \qquad k_r = \frac{1}{2}\langle u_i' u_i' \rangle = \frac{1}{2}\langle T_{ii} \rangle \tag{11}$$

$$\langle \rangle \text{ is time average operation}$$

4.1 Velocity field results

Figure 5 shows mean velocity and Reynolds stress component variation closer to the nozzle exit ($z = 1D$). LES result predicts the velocity in the cross-flow direction, U, drops upstream near $x = -0.5D$ due to the jet flow acting as an obstacle. Mean velocity components predictions, U and W, both agree very well with experimental measurements in general. Near the leeward edge of the circular nozzle ($x = 0.5D$), the negative U component is underpredicted by all three SGS models. Reynolds stress components $\overline{u'u'}$ and $\overline{w'w'}$ exhibit bimodal distribution across the jet diameter and LES result shows qualitative agreement. At such a close distance to the jet exit ($1D$ above the jet nozzle), where the flow is highly strained, LES predicted Reynolds stress components exhibit some quantitative discrepancies with experimental values. However, since all three SGS models exhibit similar Reynolds stress distributions, it can be concluded that the resolved velocity field causes this disparity. Moreover, it also shows that the imposition of inflow boundary conditions away from the jet and cross-flow interface has caused negligible disparity closer to the jet flow exit.

Figure 6 shows mean velocity predictions from three different SGS models and illustrates that the mean velocity field prediction is nearly the same for all three SGS models, and results are in very good agreement with the experimental results. The negative U velocity component at $x = 0.5D, 1D$ distances indicate the flow reversal caused behind the jet flow, and LES results have accurately predicted this phenomenon. However, as the downstream distance is increased, LES results showed overprediction in cross-flow direction velocity U. This discrepancy can be attributed to the presence of relatively
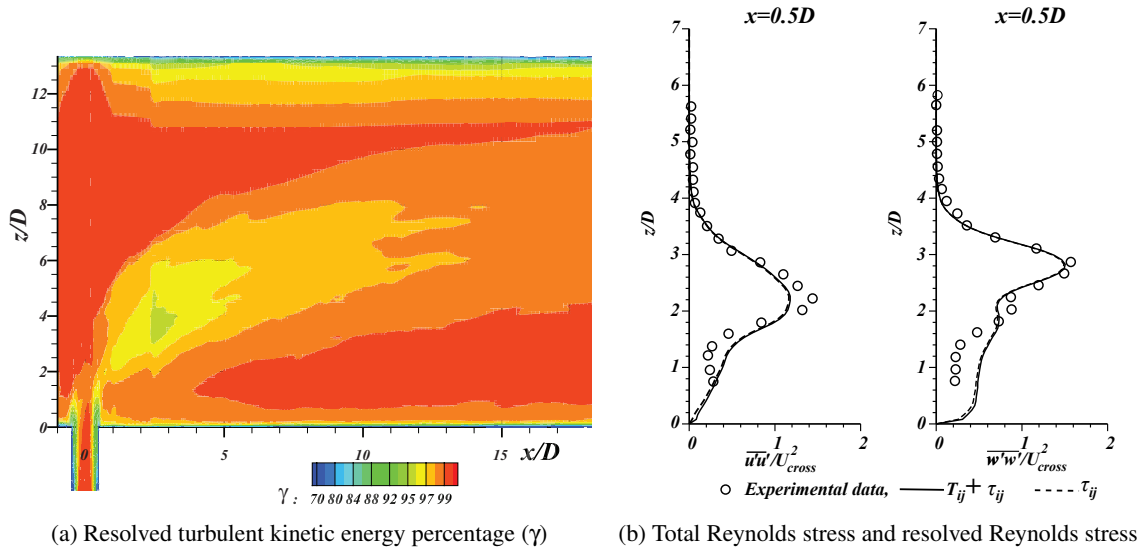
(a) Resolved turbulent kinetic energy percentage (γ)

(b) Total Reynolds stress and resolved Reynolds stress

Fig. 4: Resolved turbulent kinetic enregy percentage and Reynolds stress

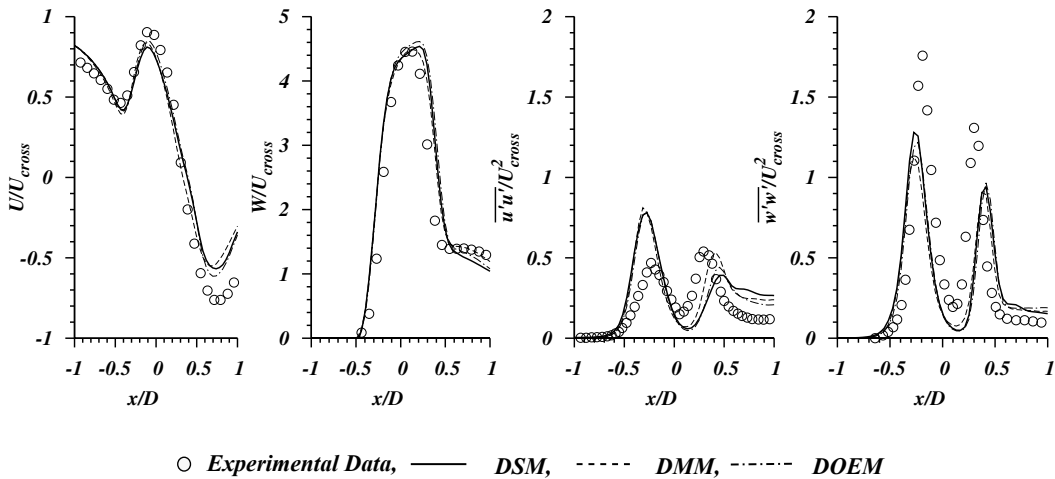
Fig. 5: Mean Velocity and Reynolds Stress component at different on $y = 0$ plane,across $z = 1D$ (Experimental data : [16])

larger eddies in size that requires more time averaging in both experimental and numerical results to obtain an accurate mean field result. The mean velocity component predictions in the jet flow direction W are consistently in very good agreement with experimental measurements. Figure 7 shows the mean velocity field contours and streamlines on a plane parallel to the cross-flow direction at $z = 1D$. It can be seen that as the cross-flow and jet-flow interacts, a high-velocity zone occurs laterally as the cross-flow attempts to flow around the jet flow. Similarly, at the leeward side of the jet, a flow reversal can be observed from both streamlines and velocity contours.

Figure 8 shows the normal Reynolds Stress components predictions $\overline{u'u'}, \overline{w'w'}$. Apart from the $x = 0D$ line which corresponds to the measurements across the jet nozzle centreline, LES results show good agreement with experimental measurements. The peak Reynolds stress strength in the stress component $\overline{u'u'}$ is in general well predicted by all three SGS model simulations. At $x = 0D$ all three SGS models show some overprediction of similar magnitude. In contrast, the peak magnitude of the Reynolds stress component $\overline{w'w'}$ at the jet centreline $x = 0D$ shows minor underprediction. Due to the strong jet deflection at this location very strong anisotropic flow strain occurs, and the LES modelling with isotropic grid filter might have caused this minor disparity. It is documented that the eddy viscosity based SGS models show deficiencies near strong mean shear fields and anisotropic turbulence [43]. Therefore, all three SGS models behave in a similar way near this high shear location of the jet deflection. The DMM model shows an increased Reynolds stress component prediction at the wall boundary of the edge of the circular jet nozzle ($x = -0.5D$, and $x = 0.5D$). Due to the lack of detailed experimental measurements it is not possible to comment on the validity of DMM model prediction. However, it is noted that high flow strains occur at this location that potentially cause flow separation and models are then prone to produce discrepancies.
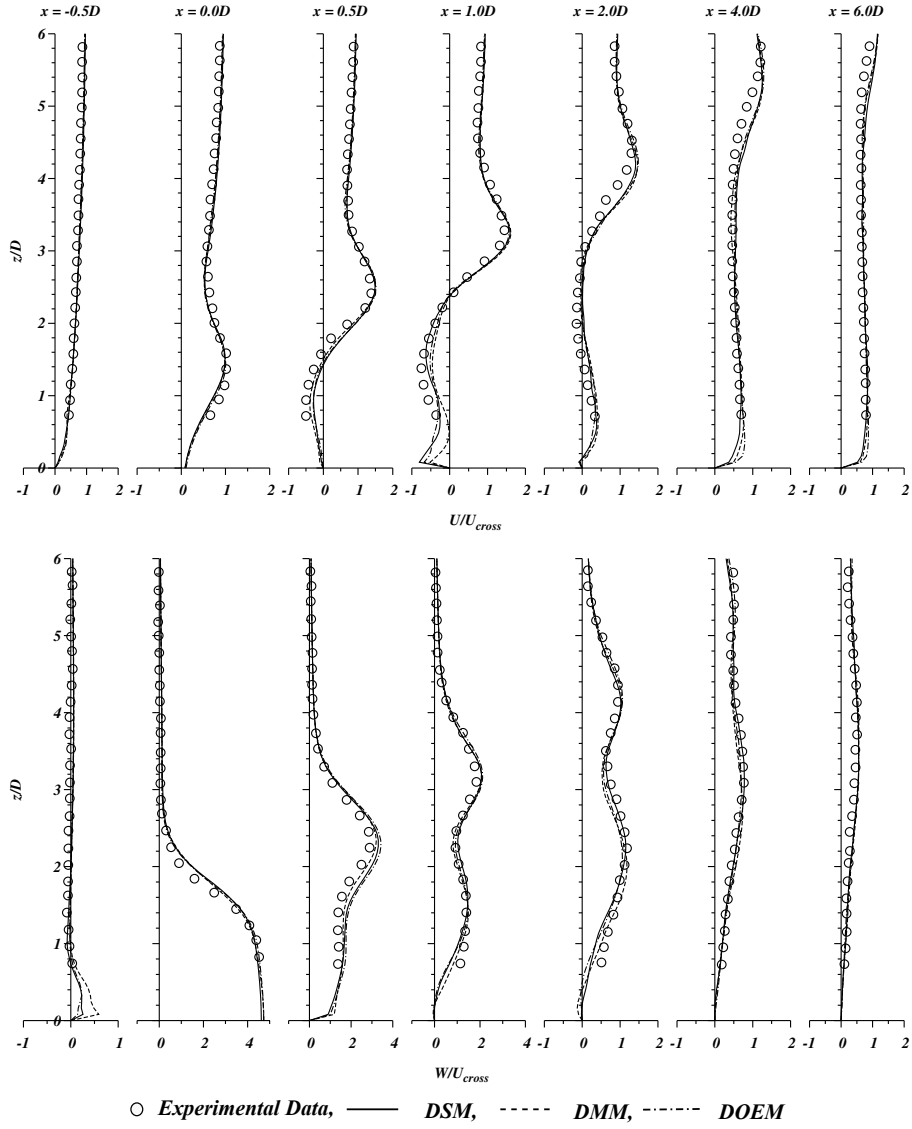
8

Fig. 6: Normalized LES mean velocity components variation on the symmetric plane. (Experimental data : [18])
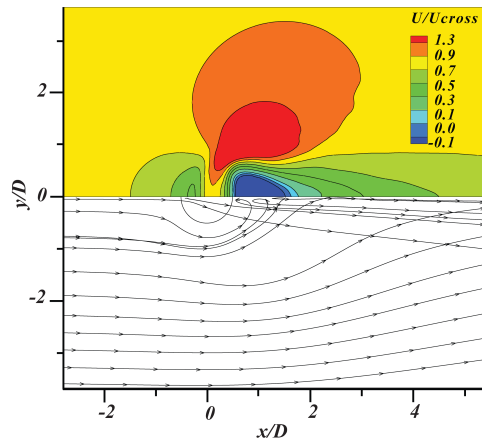

Fig. 7: Mean velocity field distribution and mean stream lines on $z = 1.5D$ plane.

9

Nevertheless, most importantly it can be seen that all three SGS models exhibit similar results in Reynolds stress field predictions. Figure 9 shows the mean velocity in the cross-flow direction U and Reynolds stress component $\overline{u'u'}$ variation at three different heights in the jet penetration direction z. Mean velocity field predictions by LES shows good agreement with experimental results; at $z = 4.5D$ a slight overprediction of LES results can be seen. Closer to the jet nozzle $z = 1.5D$ the Reynolds stress terms are slightly underpredicted in the upwind side as also shown in Figure 8. Therefore, it can be said that all three SGS models have shown very similar performance under well resolved LES resolutions.
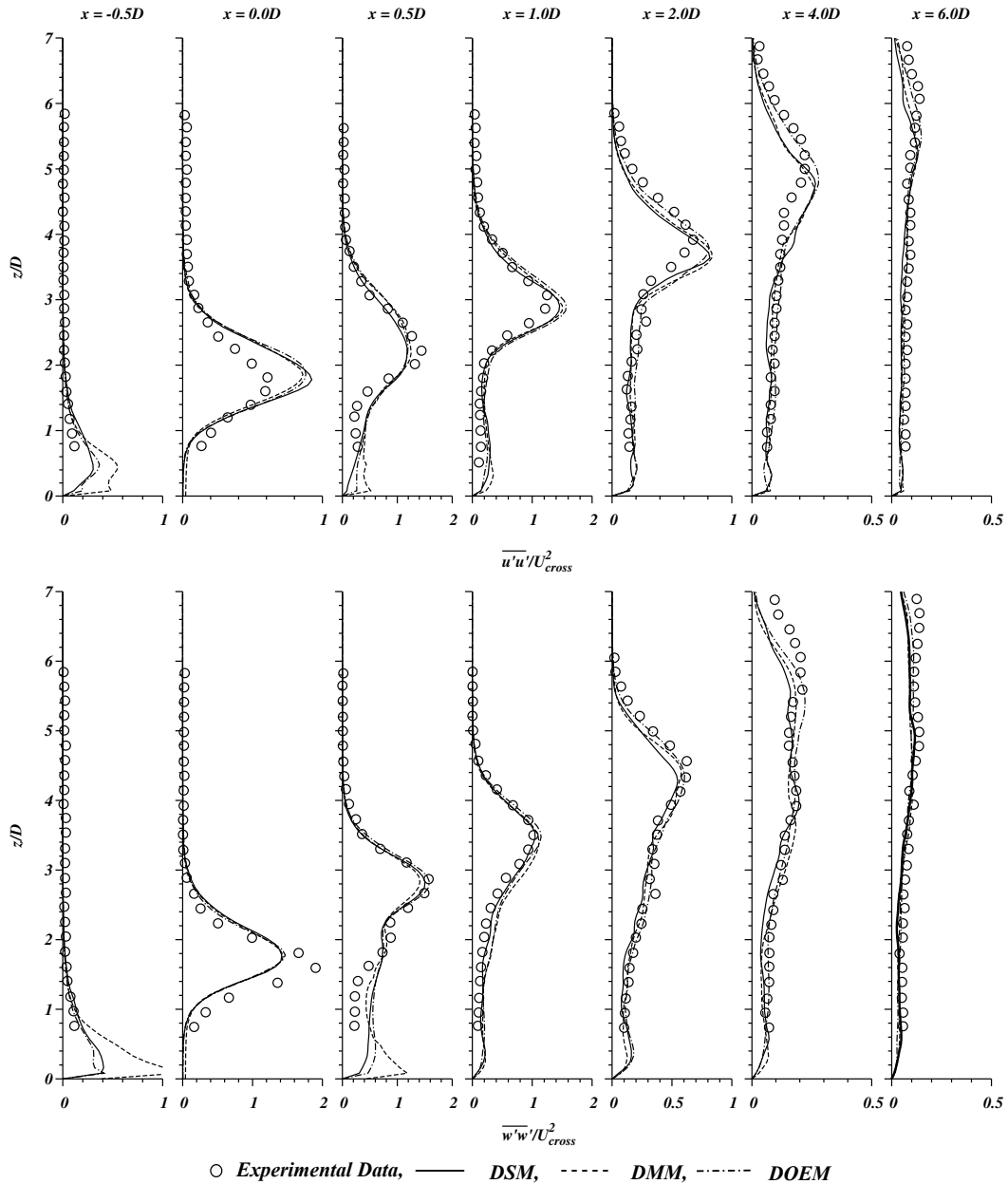
Fig. 8: Normalized mean Reynolds stress components variation on the symmetric plane $y = 0D$ (Experimental data : [18])

Since all three SGS models resulted in nearly indistinguishable results for mean velocity field and Reynolds stress field, in Figure 10 experimental results and LES predictions from the Dynamic Smagorinsky Model are compared using 2D mean velocity and Reynolds stress component contours on the $z = 1.5D$ plane. LES mean velocity field U shows an extended recirculation zone and accordingly $\overline{u'u'}$ also indicates an extended stress field distribution compared to experimental results. The LES prediction of the $\overline{v'v'}$ Reynolds stress component shows an underpredicted Reynolds stress field near the jet nozzle
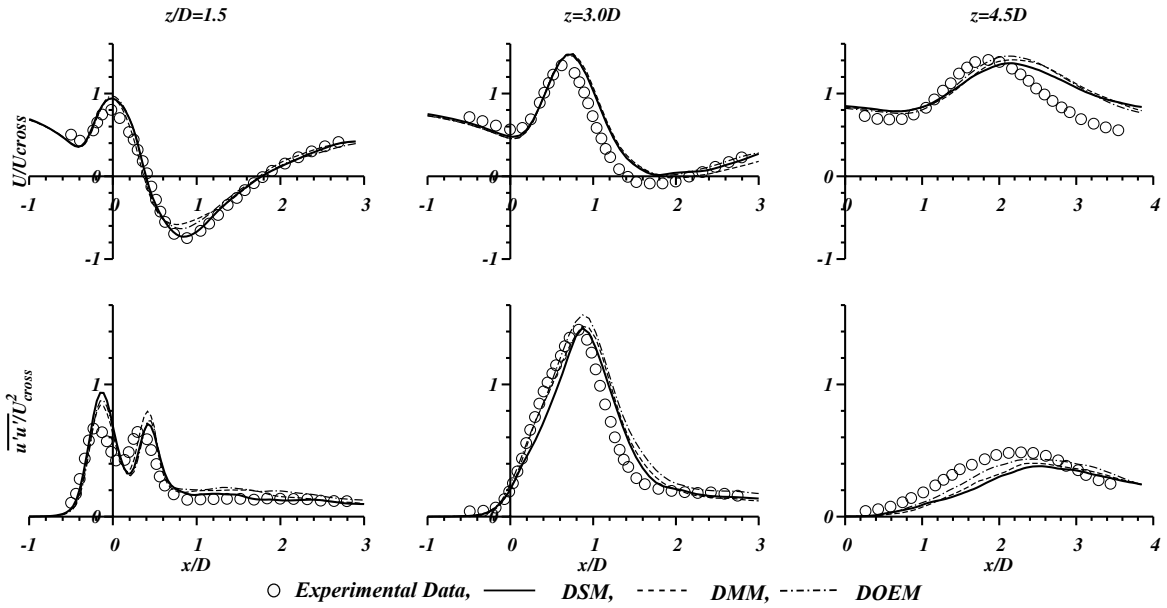
Fig. 9: Mean velocity and Reynolds stress variation in downstream direction (Experimental data : [16])

($x \approx 1D$). It is understood that to numerically resolve this flow region with intense interaction between cross-flow and jet flow a much finer grid resolution is required. The shear stress component of the Reynolds stress field $\overline{u'v'}$ also shows good overall agreement with experimental results except for the near vicinity of the jet exit ($x, y \lesssim 1D$)where the stress field values are underpredicted. Apart from these discrepancies, it can be seen that the overall momentum field predictions of LES simulations are in good agreement with experimental data.

4.2 Passive scalar mixing

Investigation of passive scalar mixing is one of the primary objectives of this study as the turbulence flow field acts as the dominant mechanism of scalar mixing. Calculated passive scalar mixing field using different SGS models are plotted in the form of mean passive scalar concentration at different downstream locations and are shown in Figure 11. As it can be seen from the passive scalar predictions, the LES results show good agreement with experimental measurements and different SGS models produce virtually indistinguishable results. This can be expected because all SGS models produce very similar turbulent velocity field results. However, all three SGS models predict a slight underprediction in the peak passive scalar concentration in the $1D \leqslant x \leqslant 3D$. The gradient diffusion hypothesis used for the sub-grid scalar flux closure is known to produce errors as Reynolds number increase and the implicit filter size becomes larger than dissipative scales [44]. Also weakness of the gradient diffusion hypothesis based scalar flux closure in modelling of highly anisotropic turbulence is documented [45]. Therefore to further improve the scalar field prediction at highly strained locations furthermore grid refinements or higher order scalar flux closure methods needs to be investigated.

From the passive scalar concentration profiles, it can be seen that the path of the jet flow is reproduced accurately by LES results. However, at downstream locations, the passive scalar prediction show minor underpredictions which could have been potentially caused by numerical dissipation. The standard deviation of scalar concentration also agrees well with experimental results as shown in Figure 12. Although the maximum scalar concentration is underpredicted by LES simulations as the jet penetration height increases, the location where the peak concentration occurs is well predicted. However, contour plots in Figure 13 indicate that the passive scalar prediction using LES exhibits more scalar diffusion than experimental data. In LES results, the passive scalar concentration contours clearly show the effect of the counter-rotating vortex pair on mixing as at the core of the kidney shaped vortex pair high scalar concentrations exist and at the outer edges the scalar concentration decays.

5 Coherent structures and scalar mixing

The jet and cross-flow interaction generate a turbulent velocity field with complex vortex structures, these vortex structures can be categorised into four main types as,

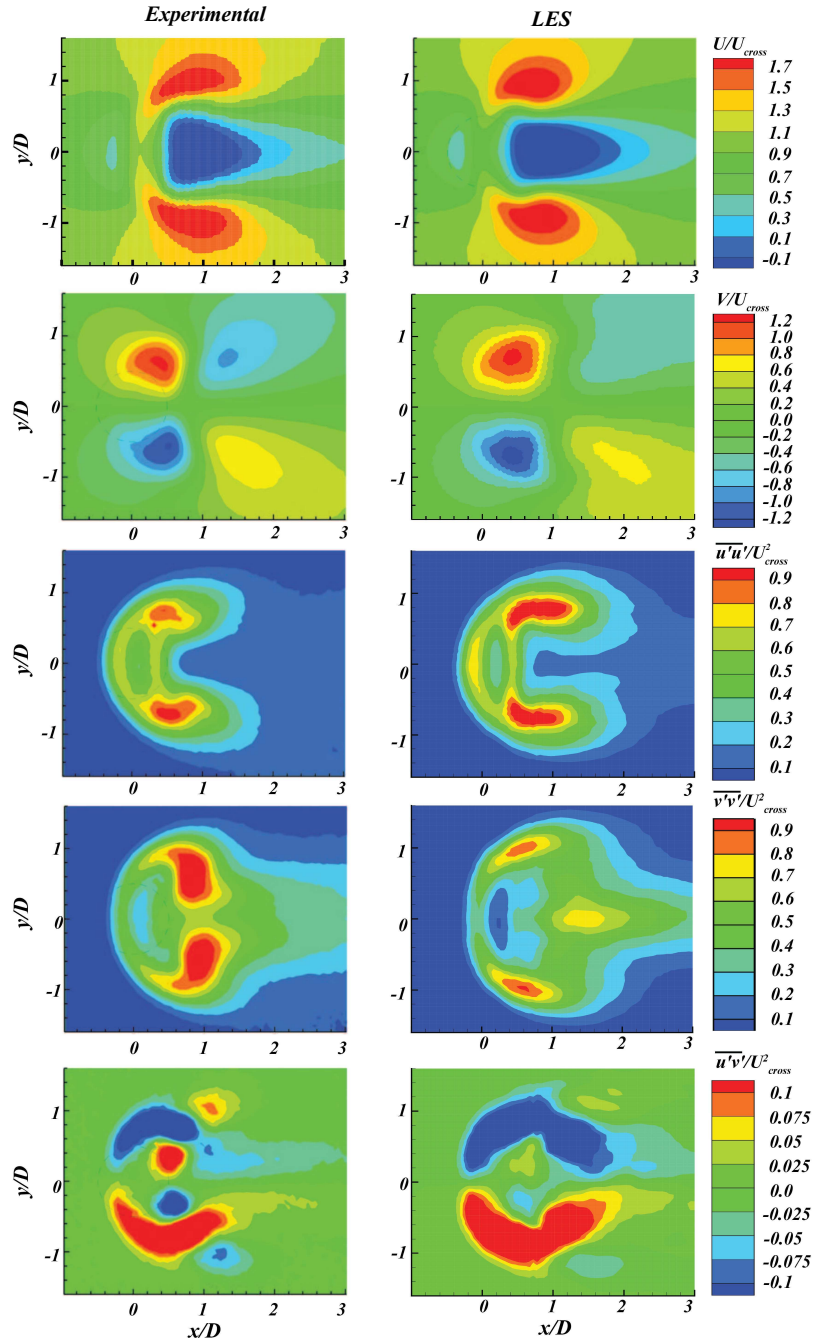1. Counter-Rotating Vortex Pair (CVP),
2. Wake vortices,

11

Fig. 10: Mean Velocity field and Reynolds stress field at $z = 1.5D$, Left : Experimental data [16], Right : DSM

3. Jet shear layer vortices,
4. Horseshoe vortices.

and these vortices are depicted in Figure 14 (Redrawn from Fric and Roshko [46]). These vortex structures are connected to each other because they all originate and are influenced by the interaction between jet flow and cross-flow. Also, these complex vortex structures cannot be considered random because of their spatial and temporal coherence; therefore they are sometimes known as coherent structures. Since the LES technique resolves eddies larger than filter scale, these coherent structures can be resolved, and in this work, the LES results are used to realise these coherent structures.

Jet shear-layer vortices are unsteady structures formed by the Kelvin-Helmholtz instability of the annular shear layer that separates from the circular jet nozzle. The horseshoe vortices that can be seen as vortex rings wrapped around the base of the jet flow are similar flow structures that can be seen at the base of a flow around a cylinder. Although horseshoe vortices
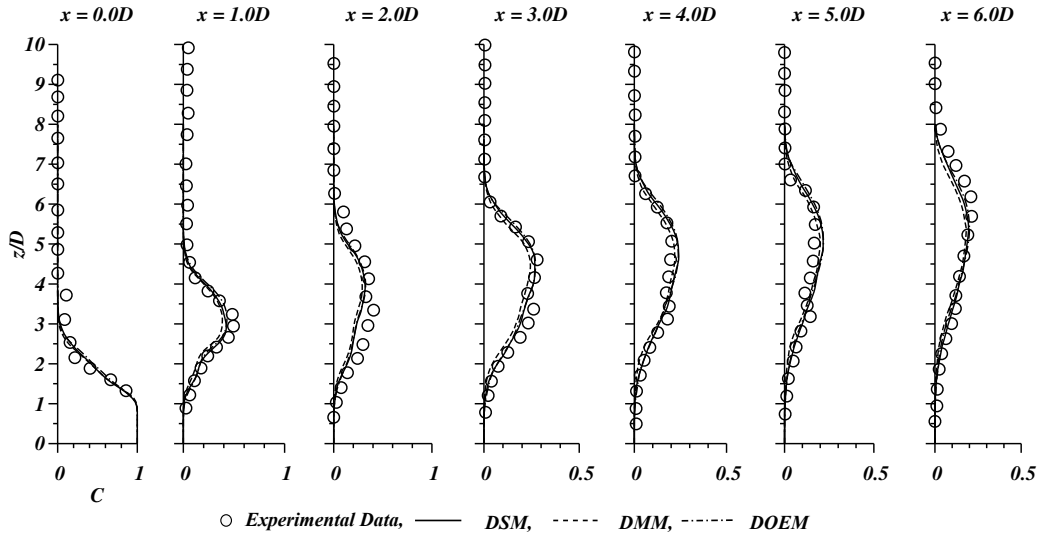
Fig. 11: Passive scalar concentration variation in z direction with increasing downstream distance (Experimental data : [17])
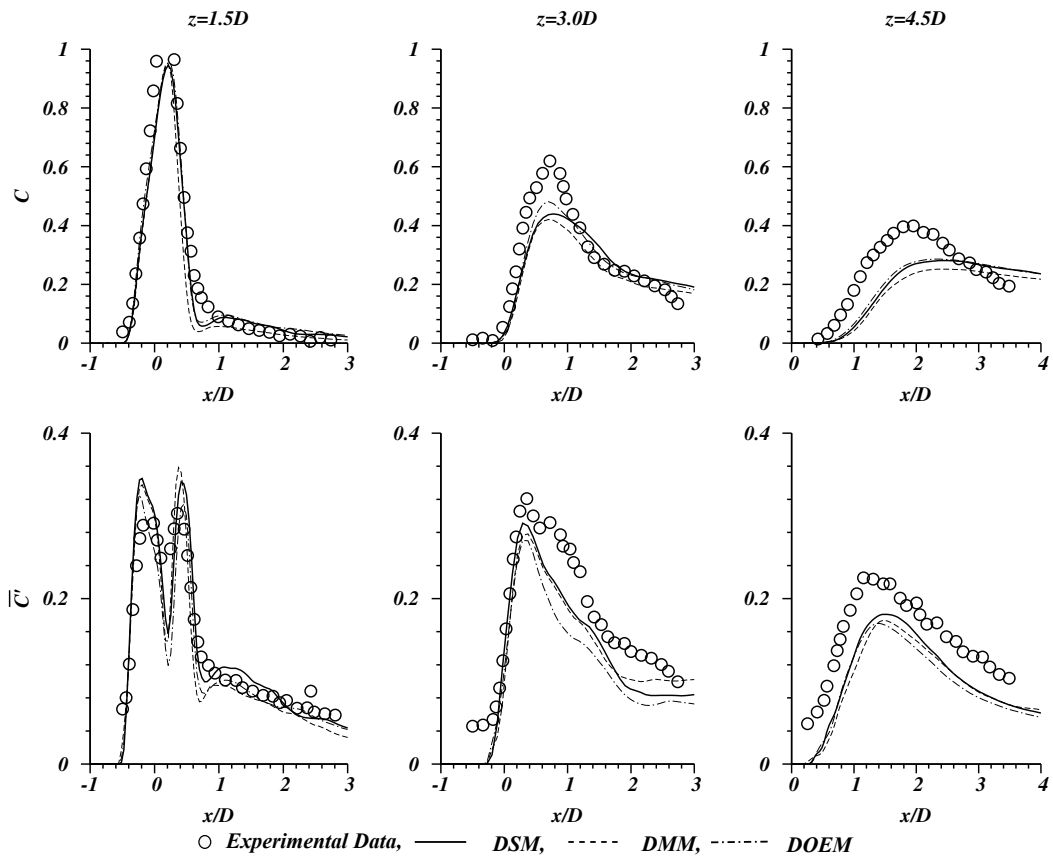
Fig. 12: Passive scalar concentration variation in x direction with increasing jet diretion distance (Experimental data : [16])

exhibit unsteadiness [47], in general, this vortex can be considered to have a mean flow feature that remains stationary surrounding the jet nozzle. Wake vortices that can be seen as vertical tornado like structures connecting the emanating jet core and the wall boundary are inherently transient vortices. Fric and Roshko [46] found through experimental investigations that the formation of these wake vortices is different from vortex shedding behind cylinders. In contrast to wakes behind solid bodies, the cross-flow shows no separation from the jet and does not exhibit vorticity shedding in the wake. They proposed that the wake vortices originate because of the separation of the wall boundary layer of the cross-flow channel. The
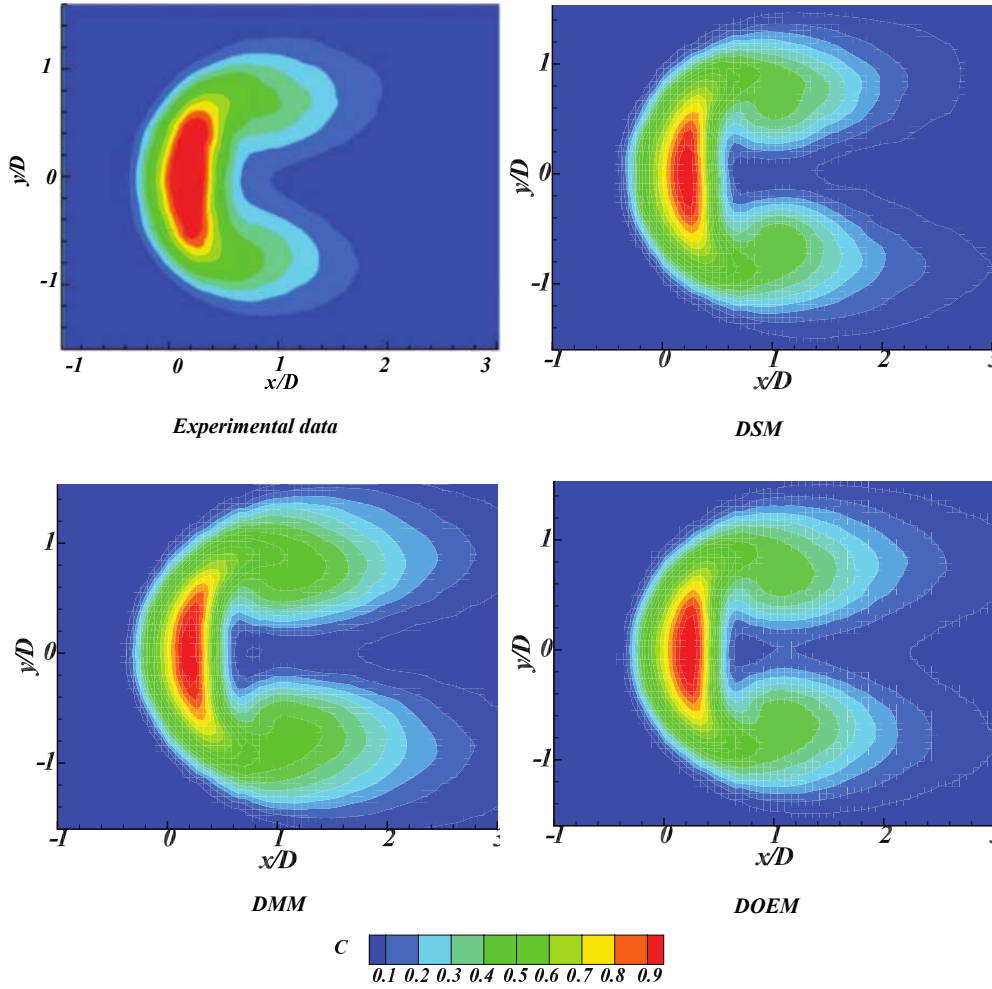
Fig. 13: Mean passive scalar contours on $z = 1.5D$ plane (Experimental data : [16])

boundary layer separation occurs on sides of the jet because of the adverse pressure gradient caused by the high-pressure zone at the leeward side of the jet. The Counter-rotating Vortex Pair (CVP) which is a unique vortex structure with a mean flow characteristic is not only entraining cross-flow air with the core of the jet flow but also dissipate the jet flow scalar towards the cross flow. There are many different theoretical explanations postulated on the exact mechanism of the CVP formation [48] [49], but all these explanations concur that the jet shear-layer is the origin of this vortex structure. Using experimental observations Kelso et al. [49] proposed that superposition of folded and rolled jet shear layer, and the mean reorientation of the shear layer vorticity contribute to the formation of CVP. LES simulations of Yuan et al. [29] postulated a different point of view of CVP formation by identifying quasi-stable hanging vortices that are formed in skewed mixing layers that occur at the lateral edges of the jet. They proposed that these hanging vortices transport the vortex strength towards the leeward side of the jet, where due to compressive stress, vortex breakdown occurs thus leading to the formation of CVP. However, through vortex method based numerical simulations, Cortelezzi and Karagozian [50] confirmed the CVP formation mechanism of Kelso et al. [49]. In another study, however, Lim et al. [51] showed experimental evidence that supports the CVP formation mechanism of Yuan et al. Therefore, the exact formation of CVP is debatable.

Since LES method resolves the eddies larger than the grid filer, the resolved velocity field can be used to realize these coherent structures and understand their effect on the mixing field. The λ2 criteria proposed by Jeong and Hussain [52] identify vortex cores by seeking local pressure minima. In this method, a vortex core is defined by the presence of two negative eigenvalues for the Hessian of pressure. Therefore a vortex structure can be identified by the presence of the negative second largest eigenvalue λ2. Figure 15 shows a negative λ2 iso-surface that shows vortex structures, and the horizontal tubular like iso-surface at the front side of the jet envelope shows the effect of the jet shear layer. Similarly, the vertically aligned iso-surface tubes indicate the wake vortex structures that connect the jet envelope and the boundary layer. These wake vortices were found to transport the passive scalar from the main jet envelope towards the wall boundary and enhance the mixing process.
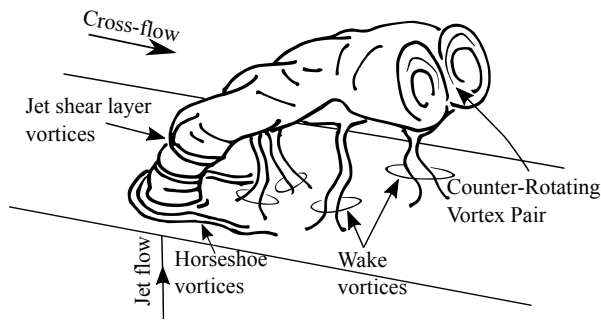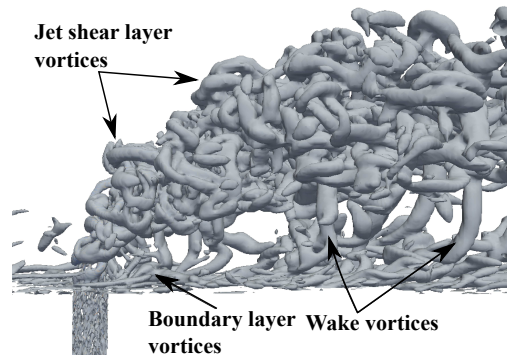
Fig. 14: Vortex structures of JICF.

Fig. 15: Vortex structures realized using λ2 criteria.

In Figure 16a the instantaneous passive scalar concentration distribution is shown on the symmetry plane and the influence of jet-shear layer vortices on the distribution of passive scalar concentration. Furthermore, it can be seen that beyond $x = 4D$, in this case, the passive scalar concentration decays faster, and this can be attributed to the dissipation of the vortices that carries the jet flow concentration. Figure 16 shows the mean passive scalar distribution and the standard deviation ($\overline{C'}$)of passive scalar distribution at a plane normal to the crossflow direction at $x = 3D$, and the effects of the counter-rotating vortex pair can be seen in the passive scalar distribution in the form of a kidney shape distribution. In the core of the counter-rotating vortex pair, the passive scalar concentration is highest, and the standard deviation is lower than the region next to the core, therefore indicating that the counter-rotating vortex pair is conserving the passive scalar concentration at its core. From the passive scalar standard deviation contours, it can be seen that the greatest passive scalar concentration fluctuations occur towards the outer layer of the CVP as expected. Figure 17 shows the instantaneous passive scalar gradients in cross-flow direction on the symmetry plane (y=0D) and on a plane normal to jet flow direction $z = 3D$. From the passive scalar gradient contour it can be seen that strong scalar gradients occur in the near field region but even at the far field there exist pockets of scalar gradient zones as a result of scalar transport via coherent structures. These scalar field results indicate that the mean scalar field shows spatial and temporal fluctuations because of the coherent structures that transport the jet flow.
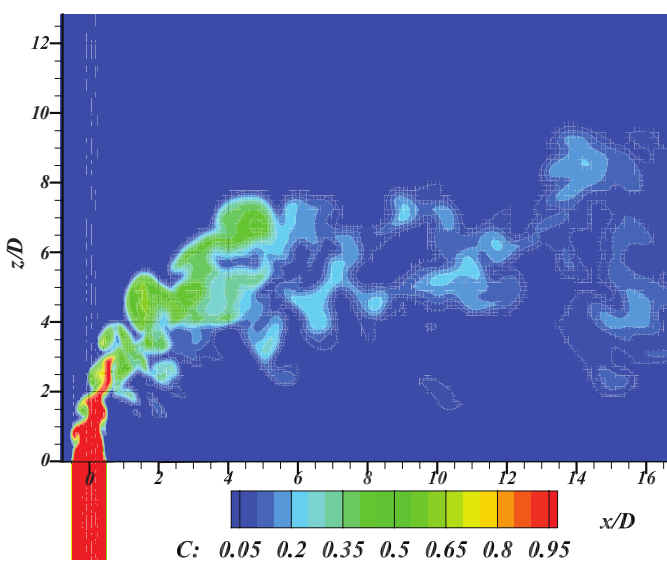
(a) Passive scalar concentration on the symmetry plane ($y = 0D$)
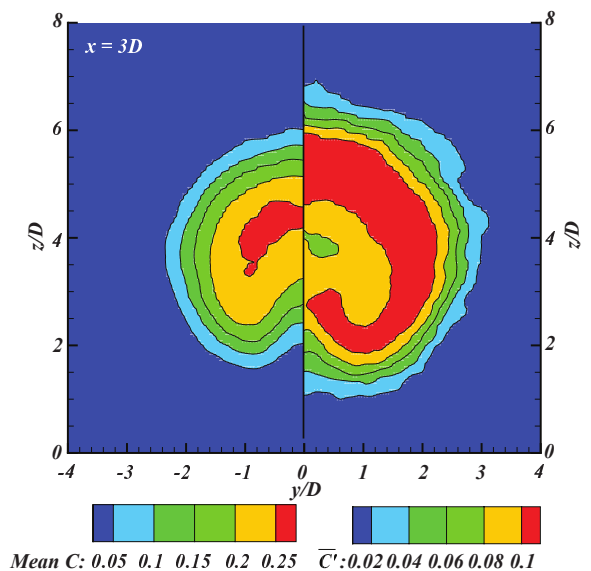
(b) Mean and Standard deviation of passive scalar concentration on the plane $x = 3D$
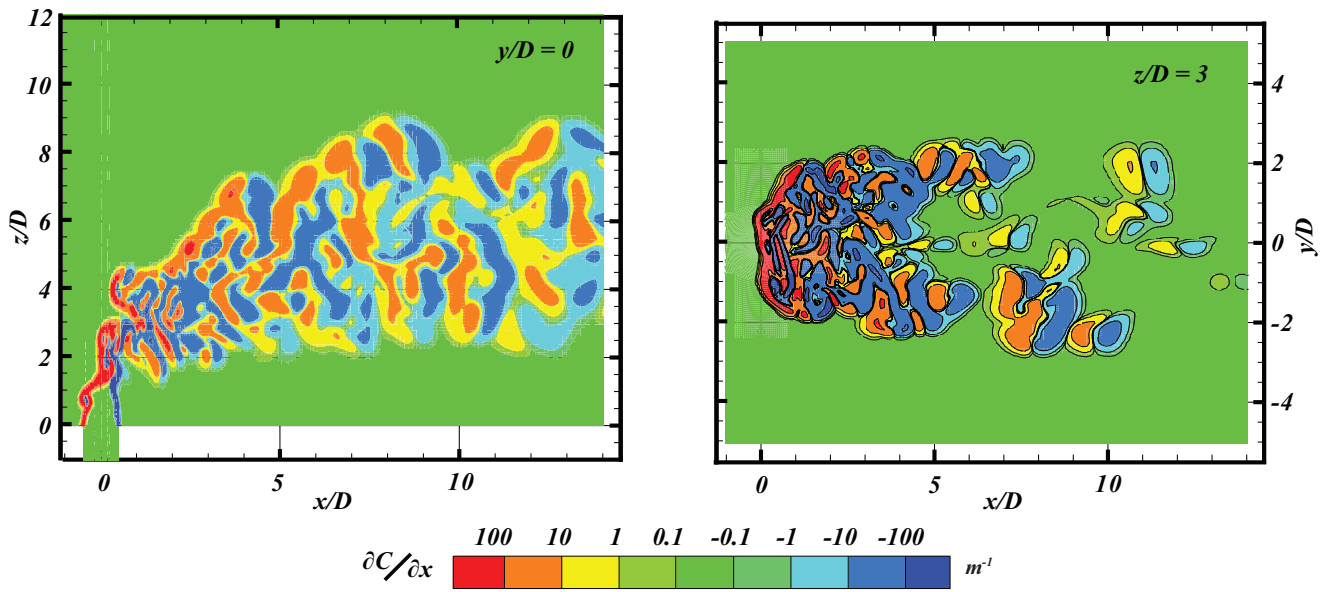
Fig. 16: Passive scalar field distribution.

Fig. 17: Passive scalar gradient in cross-flow direction.

6 Conclusions and discussion

Scalar mixing in Jet in Cross-Flow is an important area of research, especially in the field of gas turbine air-fuel mixing applications. In this study, we have used LES with different dynamic sub-grid scale stress models to investigate the Jet in Cross-Flow velocity field and scalar mixing field. The open source CFD code OpenFOAM has been used to conduct all simulations of this study. The Dynamic Smagorinsky Model (DSM), Dynamic Mixed Model (DMM), and Dynamic One Equation Model (DOEM) were compared against experimental measurements of the mean velocity field and Reynolds stress field data of the test case by Galeazzo et al. [16, 18] and Cárdenas [17]. On a computational grid with more than 85% turbulent kinetic energy resolved, all three SGS models showed very good agreement with experimental measurements in predicting both mean velocity field and Reynolds stress field. Although, there exist velocity discrepancies at the upwind and leeward corner edges of the jet nozzle where strong flow strains occur, further high-resolution velocity measurements are required to comment on the accuracy of LES modelling at these locations. Reynolds stress predictions at the highly strained locations showed discrepancies using all three SGS models. The three SGS models showed similar formations in the use of eddy viscosity hypothesis and these discrepancies can be attributed to the inadequacies of eddy viscosity based SGS models to predict high shear and anisotropic turbulence. However it can be seen that when the turbulent kinetic energy field is resolved more than 85% the effects of sub-grid stresses predicted by different models have produced similar effects. Scalar field predictions showed slightly more diffusion compared to experimental measurements, but the overall mean scalar field and the standard deviation of the scalar field results were very well represented by LES predictions. LES velocity field results can be used to extract important information like the effects of coherent structures on scalar mixing. According to both velocity field and scalar field results, it can be seen that the discrepancies between experimental measurements and simulated data are mostly concentrated in the near field of the jet and in downstream locations the experimental measurements agreed better with LES results. Therefore the LES technique can be recommended in the design optimization of air fuel mixing applications that use jet in cross-flow arrangement. This study further confirms that the OpenFOAM framework can be used very successfully to perform LES simulations to produce accurate results.

References

[1] Lyons, V. J., 1982. "Fuel air nonuniformity-effect on nitric oxide emissions". AIAA journal, **20**(5), pp. 660–665.

[2] Fric, T. F., 1993. "Effects of fuel-air unmixedness on NO(x) emissions". Journal of Propulsion and Power, **9**(5), pp. 708–713.

[3] Margason, R. J., 1993. "Fifty years of jet in cross flow research". In AGARD, Computational and Experimental Assessment of Jets in Cross Flow 41 p (SEE N94-28003 07-34), Vol. 1.

[4] Hoda, A., and Acharya, S., 2000. "Predictions of a Film Coolant Jet in Crossflow With Different Turbulence Models". Journal of Turbomachinery, **122**(3), jul, pp. 558–569.

[5] Bouchez, J.-P., and Goldstein, R., 1975. "Impingement cooling from a circular jet in a cross flow". International Journal of Heat and Mass Transfer, **18**(6), pp. 719 – 730.

[6] Schlüter, J., and Schönfeld, T., 2000. "LES of Jets in Cross Flow and Its Application to a Gas Turbine Burner". Flow, Turbulence and Combustion, **65**(2), Nov, pp. 177–203.

[7] Keffer, J. F., and Baines, W. D., 1963. "The round turbulent jet in a cross-wind". Journal of Fluid Mechanics, **15**(4), p. 481496.

[8] Ramsey, J. W., and Goldstein, R. J., 1971. "Interaction of a Heated Jet With a Deflecting Stream". Journal of Heat Transfer, **93**(4), nov, pp. 365–372.

[9] Kamotani, Y., and Greber, I., 1972. "Experiments on a turbulent jet in a cross flow". AIAA journal, **10**(11), pp. 1425–1429.

[10] Crabb, D., Durao, D., and Whitelaw, J., 1981. "A round jet normal to a crossflow". Journal of Fluids Engineering, **103**(1), pp. 142–153.

[11] Andreopoulos, J., and Rodi, W., 1984. "Experimental investigation of jets in a crossflow". Journal of Fluid Mechanics, **138**, pp. 93–127.

[12] Smith, S., Lozano, A., Mungal, M., and Hanson, R., 1993. "Scalar mixing in the subsonic jet in crossflow". In AGARD, Computational and Experimental Assessment of Jets in Cross Flow 13 p (SEE N94-28003 07-34), Vol. 1.

[13] Smith, S. H., and Mungal, M. G., 1998. "Mixing, structure and scaling of the jet in crossflow". Journal of Fluid Mechanics, **357**, pp. 83–122.

[14] Su, L. K., and Mungal, M. G., 2004. "Simultaneous measurements of scalar and velocity field evolution in turbulent crossflowing jets". Journal of Fluid Mechanics, **513**, aug, pp. 1–45.

[15] Cárdenas, C., Suntz, R., Denev, J. A., and Bockhorn, H., 2007. "Two-dimensional estimation of Reynolds-fluxes and-stresses in a Jet-in-Crossflow arrangement by simultaneous 2D-LIF and PIV". Applied physics B, **88**(4), pp. 581–591.

[16] Galeazzo, F. C. C., Donnert, G., Habisreuther, P., Zarzalis, N., Valdes, R. J., and Krebs, W., 2011. "Measurement and simulation of turbulent mixing in a jet in crossflow". Journal of Engineering for Gas Turbines and Power, **133**(6), pp. 061504–061504–10.

[17] Cardenas, C., Sedlmaier, J., Zarzalis, N., Valdes, R. J., and Krebs, W., 2011. "Measurement of a benchmarking jet in crossflow configuration under highly turbulent conditions". In ASME 2011 Turbo Expo: Turbine Technical Conference and Exposition, American Society of Mechanical Engineers, pp. 51–60.

[18] Galeazzo, F. C. C., 2013. "Simulation of turbulent flows with and without combustion with emphasis on the impact of coherent structures on the turbulent mixing". PhD thesis, KIT - Karlsruher Institut für Technologie.

[19] Ivanova, E. M., Noll, B. E., and Aigner, M., 2012. "A Numerical Study on the Turbulent Schmidt Numbers in a Jet in Crossflow". Journal of Engineering for Gas Turbines and Power, **135**(1), nov, pp. 011505–10.

[20] Ivanova, E. M., Noll, B. E., and Aigner, M., 2011. "Computational Modeling of Turbulent Mixing of a Transverse Jet". Journal of Engineering for Gas Turbines and Power, **133**(2), pp. 021505–7.

[21] Patankar, S. V., Basu, D. K., and Alpay, S. A., 1977. "Prediction of the Three-Dimensional Velocity Field of a Deflected Turbulent Jet". Journal of Fluids Engineering, **99**(4), dec, pp. 758–762.

[22] Alvarez, J., Jones, W. P., and Seoud, R., 1993. "Predictions of momentum and scalar fields in a jet in cross-flow using first and second order turbulence closures". In In AGARD, Computational and Experimental Assessment of Jets in Cross Flow 10 p (SEE N94-28003 07-34), Vol. 1.

[23] Launder, B., and Samaraweera, D., 1979. "Application of a second-moment turbulence closure to heat and mass transport in thin shear flows–I. Two-dimensional transport". International Journal of Heat and Mass Transfer, **22**(12), pp. 1631–1643.

[24] Jones, W., and Wille, M., 1996. "Large-eddy simulation of a plane jet in a cross-flow". International Journal of Heat and Fluid Flow, **17**(3), June, pp. 296–306.

[25] Smagorinsky, J., 1963. "General circulation experiments with the primitive equations: I. The basic experiment". Monthly Weather Review, **91**(3), mar, pp. 99–164.

[26] Piomelli, U., and Liu, J., 1995. "Large-eddy simulation of rotating channel flows using a localized dynamic model". Physics of Fluids, **7**(4), pp. 839–848.

[27] Schmidt, H., and Schumann, U., 1989. "Coherent structure of the convective boundary layer derived from large-eddy simulations". Journal of Fluid Mechanics, **200**, pp. 511–562.

[28] Chen, K. S., and Hwang, J. Y., 1991. "Experimental study on the mixing of one- and dual-line heated jets with a cold crossflow in a confined channel". AIAA Journal, **29**(3), Mar., pp. 353–360.

[29] Yuan, L. L., Street, R. L., and Ferziger, J. H., 1999. "Large-eddy simulations of a round jet in crossflow". Journal of Fluid Mechanics, **379**, p. 71104.

[30] Sherif, S. A., and Pletcher, R. H., 1989. "Measurements of the Flow and Turbulence Characteristics of Round Jets in Crossflow". Journal of Fluids Engineering, **111**(2), pp. 165–171.

[31] Zang, Y., Street, R. L., and Koseff, J. R., 1993. "A dynamic mixed subgridscale model and its application to turbulent recirculating flows". Physics of Fluids A: Fluid Dynamics, **5**(12), pp. 3186–3196.

[32] Majander, P., and Siikonen, T., 2006. "Large-eddy simulation of a round jet in a cross-flow". International Journal of Heat and Fluid Flow, **27**(3), pp. 402–415.

[33] Salewski, M., Stankovic, D., and Fuchs, L., 2008. "Mixing in Circular and Non-circular Jets in Crossflow". Flow, Turbulence and Combustion, **80**(2), jan, pp. 255–283.

[34] Galeazzo, F. C. C., Donnert, G., Cárdenas, C., Sedlmaier, J., Habisreuther, P., Zarzalis, N., Beck, C., and Krebs, W., 2013. "Computational modeling of turbulent mixing in a jet in crossflow". International Journal of Heat and Fluid Flow, **41**, pp. 55–65.

[35] Germano, M., Piomelli, U., Moin, P., and Cabot, W. H., 1991. "A dynamic subgrid-scale eddy viscosity model". Physics of Fluids A: Fluid Dynamics, **3**(7), July, p. 1760.

[36] Lilly, D. K., 1992. "A proposed modification of the Germano subgrid-scale closure method". Physics of Fluids A: Fluid Dynamics, **4**(3), mar, p. 633.

[37] Vreman, B., Geurts, B., and Kuerten, H., 1994. "On the formulation of the dynamic mixed subgridscale model". Physics of Fluids, **6**(12), pp. 4057–4059.

[38] Kornev, N. V., Tkatchenko, I. V., and Hassel, E., 2005. "A simple clipping procedure for the dynamic mixed model based on Taylor series approximation". Communications in Numerical Methods in Engineering, **22**(1), July, pp. 55–61.

[39] Fureby, C., Tabor, G., Weller, H. G., Gosman, A. D., and Tabor, . G., 1997. "A comparative study of subgrid scale models in homogeneous isotropic turbulence". Physics of Fluids Physics of Fluids A: Fluid Dynamics, **9**(4), pp. 1416–1492.

[40] de Villiers, E., 2006. "The potential of large-eddy simulation for the modelling of wall bounded flows". PhD thesis, Imperial College of Science, Technology and Medicine.

[41] Spalding, D. B., 1961. "A Single Formula for the Law of the Wall". Journal of Applied Mechanics, **28**(3), sep, pp. 455–458.

[42] Pope, S. B., 2004. "Ten questions concerning the large-eddy simulation of turbulent flows". New Journal of Physics, **6**(1), Mar., pp. 35–35.

[43] Lévêque, E., Toschi, F., Shao, L., and Bertoglio, J.-P., 2007. "Shear-improved smagorinsky model for large-eddy simulation of wall-bounded turbulent flows". Journal of Fluid Mechanics, **570**, pp. 491–502.

[44] da Silva, C. B., and Pereira, J. C., 2007. "Analysis of the gradient-diffusion hypothesis in large-eddy simulations based on transport equations". Physics of Fluids, **19**(3), p. 035106.

[45] Combest, D. P., Ramachandran, P. A., and Dudukovic, M. P., 2011. "On the Gradient Diffusion Hypothesis and Passive Scalar Transport in Turbulent Flows". Industrial & Engineering Chemistry Research, **50**(15), aug, pp. 8817–8823.

[46] Fric, T. F., and Roshko, A., 1994. "Vortical structure in the wake of a transverse jet". Journal of Fluid Mechanics, **279**, pp. 1–47.

[47] Kelso, R. M., and Smits, A. J., 1995. "Horseshoe vortex systems resulting from the interaction between a laminar boundary layer and a transverse jet". Physics of Fluids, **7**(1), pp. 153–158.

[48] Andreopoulos, J., 1985. "On the structure of jets in a crossflow". Journal of Fluid Mechanics, **157**, pp. 163–197.

[49] Kelso, R. M., Lim, T., and Perry, A., 1996. "An experimental study of round jets in cross-flow". Journal of fluid mechanics, **306**, pp. 111–144.

[50] Cortelezzi, L., and Karagozian, A. R., 2001. "On the formation of the counter-rotating vortex pair in transverse jets". Journal of Fluid Mechanics, **446**, pp. 347–373.

[51] Lim, T. T., New, T. H., and Luo, S. C., 2001. "On the development of large-scale structures of a jet normal to a cross flow". Physics of Fluids, **13**(3), mar, pp. 770–775.

[52] Jeong, J., and Hussain, F., 1995. "On the identification of a vortex". Journal of Fluid Mechanics, **285**, pp. 69–94.

List of Tables

List of Figures